ERDC MSRC/PET TR/00-37

On Coupling the SWAN and WAM Wave Models for Accurate Nearshore Wave Predictions

by

Stephen F. Wornom
David J.S. Welsh
Keith W. Bedford

1 August 2000

Work funded by the DoD High Performance Computing Modernization Program ERDC Major Shared Resource Center through

Programming Environment and Training (PET)

Supported by Contract Number: DAHC94-96-C0002
CSC Nichols

On Coupling the SWAN and WAM Wave Models for Accurate Nearshore Wave Predictions

Stephen F. Wornom
U.S. Army Engineer Research and Development Center
Major Shared Resource Center, Vicksburg, Mississippi
The Ohio State University PET CWO Lead
and
David J. S. Welsh, Keith W. Bedford
Department of Civil and Environmental Engineering and Geodetic Science
The Ohio State University

August 1, 2000

On Coupling the SWAN and WAM Wave Models for Accurate Nearshore Wave Predictions

Topic: Nearshore Wave Predictions

Authors
Stephen F. Wornom, Research Scientist
U.S. Army Engineer Research and Development Center
ATTN: CEERD-IH-C Dr. Stephen Wornom
3909 Halls Ferry Road
Vicksburg, MS 39180-619
address all correspondance to this author

Tel: 601-634-4663
Fax: 601-634-3808
e-mail: wornomsf@wes.hpc.mil

David J. S. Welsh, Research Scientist
Department of Civil and Environmental Engineering and Geodetic Science
The Ohio State University
2070 Neil Avenue
Columbus,Ohio 43210

Tel: 614-292-6919
Tel: 614-292-3780
e-mail: welsh.1@superior.eng.ohio-state.edu

Keith W. Bedford, Professor and Chair
Department of Civil and Environmental Engineering and Geodetic Science
The Ohio State University
2070 Neil Avenue
Columbus,Ohio 43210

Tel: 614-292-3808
Tel: 614-292-3780
e-mail: bedford.1@osu.edu

On Coupling the SWAN and WAM Wave Models for Accurate Nearshore Wave Predictions

Abstract

A simulation of wind-wave activity during 1995 Hurricane Luis has been performed using the WAM and SWAN wave models. This study tested the WAM/SWAN interface option present in the SWAN code to determine the effectiveness of applying SWAN in the finest WAM nest as a means to obtain more accurate nearshore wave predictions. The SWAN code was developed specifically for the nearshore and contains formulations for two physical processes not represented in the WAM code: depth-induced wave breaking and triad wave-wave interaction. SWAN was run with and without these processes to determine their effects on the results. The inclusion of triad wave-wave interaction did not significantly affect the results. In contrast, the inclusion of depth-induced wave breaking reduced the maximum wave height at the storm's peak by 20 percent at the test site located 900 m offshore in a water depth of 8 m. These results suggest that applying the SWAN code in the finest WAM nest can be an effective means of obtaining more accurate nearshore wave predictions.

Keywords: WAM, SWAN, nearshore wave prediction, 1995 Hurricane Luis, depth-induced wave breaking, triad wave-wave interaction.

1 Introduction

One of the major challenges in ocean modeling is the accurate prediction of nearshore wave conditions. Accurate nearshore wave conditions are necessary for environmental impact studies of erosion and sediment transport and play an equally important role in naval navigation and landing operations.

WAM (acronym for WAve Model) and SWAN (acronym for Simulating WAves Nearshore) are third-generation wave models used to compute the spectra of random short-crested wind-generated waves on Eulerian grids. The WAM code has been primarily developed to generate the open-ocean wave predictions necessary for naval operations and commercial ship movement, whereas SWAN has been developed and validated specifically for coastal and inland waters. Deepwater ocean waves are primarily wind-driven, but in nearshore zones, finite-depth effects such as bottom friction, shoaling, refraction, depth-induced breaking, and modified wave-wave interaction become important. In deep water, quadruplet wave-wave interactions dominate the wave spectrum evolution, whereas in shallow water, triad wave-wave interactions become important (Beji and Battes [3] and Arcilla et al. [1], for example) and depth-induced wave breaking may dominate all other processes. Thus, wave models like WAM, which only account for quadruplet wave-wave interaction processes and do not account for depth-induced wave-breaking, may not predict nearshore wave conditions as accurately as codes developed specifically for nearshore use.

The SWAN model includes a WAM/SWAN interface option that allows the boundary conditions for a fine-nest SWAN simulation to be provided by a coarse-nest WAM simulation. The boundary conditions are passed in the form of nonstationary energy-spectra in frequency-direction space. The purpose of this study was to test the WAM/SWAN interface option present in the SWAN code to determine the effectiveness of applying SWAN in the finest WAM nest in order to obtain more accurate nearshore wave predictions. The selected test case is a simulation of wind-wave activity during 1995 Hurricane Luis for which National Oceanic and Atmospheric Administration (NOAA) buoy and station data were available, as were data from the U.S. Army Field Research Facility (FRF) at Duck, NC. Comparison of the WAM and SWAN results with the wave observations permit evaluation of the effectiveness of applying SWAN in the finest WAM nest. These comparisons may also indicate areas where the models need to be improved.

A similar study was performed by Padilla et al. [16] for a severe North Sea storm, which occurred in February 1993. In that study, two WAM nests were employed. The coarse mesh contained 25x48 points with a cell size of 50 km and the fine mesh contained 251x241 points with a cell size of 10 km. To simplify the comparison of the WAM and SWAN results, both codes were run on a Cartesian grid. Depth-induced breaking and triad wave-wave interaction were not used for the SWAN runs.

The present study differs from the Padilla et al. [16] study in several aspects: 1) the SWAN fine mesh cell size in this study was approximately 150 m x 190 m; 2) in the finest nest where WAM was used, a Cartesian grid was used. The WAM runs on the larger nests were made using spherical wave propagation; and 3) some of the SWAN runs included depth-induced wave breaking and triad wave-wave interactions to evaluate their influence on the SWAN results.

2 Description of the SWAN and WAM codes

WAM and SWAN are third generation wave models that compute spectra of random short-crested, wind-generated waves. WAM was primarily developed for coastal and deepwater wave predictions, whereas SWAN was developed specifically for nearshore zones. Both codes can be used for shallow water and deepwater calculations and can account for unsteady current and depth fields. The following basic physics are accounted for in both codes:

- Wave propagation in time and space
- Wave generation by wind
- Shoaling and refraction due to depth
- Shoaling and refraction due to current
- Whitecapping and bottom friction
- Quadruplet wave-wave interactions

2.1 The SWAN code

The SWAN code contains formulations for two physical processes not present in the WAM code. These processes can play an important role for nearshore calculations; they are as follows:

- Depth-induced wave-breaking
- Triad wave-wave interaction

SWAN solves a spectral wave-action transport equation

$$\frac{\partial}{\partial t}\hat{E} + \frac{\partial}{\partial x}(c_x\hat{E}) + \frac{\partial}{\partial y}(c_y\hat{E}) + \frac{\partial}{\partial \sigma}(c_\sigma\hat{E}) + \frac{\partial}{\partial \theta}(c_\theta\hat{E}) = S/\sigma \tag{1}$$

where

$$S = S_{in} + S_{nl} + S_{wc} + S_{bf} + S_{dib} \tag{2}$$

and

$\hat{E}(x, y, \sigma, \theta, t)$	= wave action density spectrum
σ	= relative frequency
θ	= wave direction
$S_{in}(\sigma, \theta)$	= wind input
$S_{nl}(\sigma, \theta)$	= non-linear wave-wave interaction
$S_{wc}(\sigma, \theta)$	= dissipation due to whitecapping
$S_{bf}(\sigma, \theta)$	= dissipation due to bottom friction
$S_{dib}(\sigma, \theta)$	= depth-induced breaking
c_x, c_y	= propagation velocities in Cartesian space

SWAN uses the wave action density spectrum, $\hat{E}$, rather than the energy density spectrum, E, because in the presence of currents, the wave action density spectrum is conserved whereas the energy density spectrum is not. They are related through the relation

$$\hat{E} = E/\sigma \tag{3}$$

SWAN solves the spectral wave-action transport equation on a Cartesian mesh using a fully implicit upwind scheme in geographical space. In directional and frequency space, the level of accuracy and diffusion can be selected by the user. The implicit scheme used in geographical space is unconditionally stable and thus avoids numerical instabilities. The time-step selection is designed to accurately capture the unsteady physics rather than to maintain numerical stability. In many cases this leads to smaller CPU time requirements. However, a large time-step increases dispersion and dissipation errors. The details of the SWAN code are given by Booij et al. [4] and Ris et al. [18]. The SWAN code gives the user the option to include different physics modules. For example, there are three parameterizations for whitecapping and three for bottom friction. The different formulations can be found in the SWAN USER MANUAL [9], which can be downloaded from the SWAN Web site (http://www.swan.ct.tudelft.nl). In this study, the SWAN source terms corresponding to those in WAM Cycle 4 were used. Thus, the differences in the results for the SWAN runs, where the the triad wave-wave interaction and depth-induced wave breaking processes were switched off, and the WAM runs using a Cartesian mesh are primarily due to the different numerical algorithms and their implementation. It should be noted that the two Cartesian grids were not identical - Section 3.2.

Version 40.01 of the SWAN code contains a number of improved features. Version 40.01 has a more accurate numerical estimation of breaking waves in the surf zone. The limiter used to stabilize

the quadruplet wave-wave interactions has been modified to avoid the undue damping of triad wave-wave interactions exhibited in earlier versions of the code. Model improvements have also been made for the case of very strong refraction. An important upgrade in version 40.01 is the option to use nonstationary boundary conditions. A restart capability has also been implemented, and stationary and nonstationary computations can be made in the same run.

2.2 The WAM code

The WAM model, described in Hasslemann et al. [7], solves a spectral wave energy transport equation, shown here for spherical wave propagation, on a great circle path

$$\frac{\partial E}{\partial t} + (cos\phi)^{-1}\frac{\partial}{\partial \phi}(\dot{\phi}\ cos\phi\ E) + \frac{\partial}{\partial \lambda}(\dot{\lambda}E) + \frac{\partial}{\partial \sigma}(\dot{\sigma}E) + \frac{\partial}{\partial \theta}(\dot{\theta}E) = S_{in} + S_{wc} + S_{nl} + S_{bf} \quad (4)$$

where

$E(\phi, \lambda, \theta, \sigma, t)$	= wave energy density spectrum
ϕ	= latitude
λ	= longitude
$\dot{\phi}$	= time rate of change of ϕ
$\dot{\lambda}$	= time rate of change of λ
$\dot{\sigma}$	= time rate of change of of the relative frequency
$\dot{\theta}$	= time rate of change of the propagation direction

WAM uses an explicit first-order accurate upwind scheme in geographical space and can propagate the solution on a Cartesian mesh or a spherical grid. A consequence of the explicit scheme is that the time-step is proportional to the spatial step size. Therefore, as the mesh is refined, the time-step must be reduced to maintain stability, thus increasing the computational effort. WAM is one of the most extensively tested and widely used wave models in the world and is well documented. A detailed description of the WAM code is given by Gunther et al. [6] and Komen et al. [12]. The WAM documentation can also be found on the web (http://www.dkrz.de/forschung/reports/wamh-1-eng.html).

3 Hurricane Luis deployment

Hurricane Luis was chosen as the test case for this study. This selection was made due to the combination of high storm activity and excellent data availability. Luis was a category 4 Cape Verde

hurricane that left 16 people dead and caused 2-1/2 billion dollars in damage in the Leeward Islands. Hurricane Luis did not strike the U.S. mainland.

The different nests used in the simulation of the hurricane can be seen in Figure 1, which was the coarsest nest used and the starting nest for the simulation. The figure also shows a contour plot of the basin wind speeds on September 10, 1995, 0-UTC. This time approximately corresponds to the peak of the storm as measured at NOAA buoy 44014. At the top right of Figure 1, the date and hour of the wind speed contours is shown. Note that both the notation September 10, 1995, and 95/09/10 are used in this paper. The state of Florida can be recognized in the lower left corner of the region nest.

The path of the eye of the hurricane is also shown in Figure 1. The coordinates of the path were obtained from the NOAA Web site (http://www.nhc.noaa.gov/1995luis.html) and not from the wind fields. Another source is http://weather.unisys.com/hurricane/atlantic/1995/LUIS/track.dat); the maximum wind speeds are slightly higher from this source. Overlaying the NOAA data on contour plots of the wind speeds served to validate that the eye of the hurricane deduced from wind speed and significant wave height contour plots was consistent with the NOAA Web site data.

The simulation period for this study was Aug. 29, 0-UTC to September 13, 0-UTC. The evaluation period was taken as the 10-day period from September 3, 0-UTC to September 13, 0-UTC; the model spin-up portion of the simulation was not used for evaluation purposes.

3.1 Nested grid structure

Four WAM nests were used in the present study. The nests are referred to as the "basin" (30-minute resolution, 135x120 cells), "region" (15-minute resolution, 120x96 cells), "subregion 1 (sub1)" (5-minute resolution, 84x120 cells), and "subregion 2 (sub2)" (5/4-minute resolution; 96x96 cells), moving from coarser to finer resolution. Table 1 gives information concerning the different nests used for the WAM and SWAN computations. WAM was run on the first four nests. WAM could not be run on the sub3 nest because the time-step required was 30 seconds, whereas the minimum time-step permitted with the WAM date stamp formulation was 1 minute. The approximate mesh sizes are also given in Table 1. Table 2 shows time-step information regarding the WAM runs.

SWAN was run on the sub2, sub3, and sub4 nests. The SWAN runs on the sub2 nest were made to verify that equivalent accuracy could be achieved on this relatively large grid with either the WAM or SWAN codes. The sub2 nest covers two degrees by two degrees, which is close to the limit where a Cartesian grid can be expected to produce accurate results owing to the curvature of the Earth.

The main purpose of this study was to show that deploying the SWAN code on the finest nest

Table 1 Nest data

nest level	max/min lon. (deg)	max/min lat. (deg)	resol. (min)	approx. mesh size (km)
basin	345/277.5	70/10	30	54.7 km
region	308/278	48/24	15	25.4 km
sub1	290/283	41/31	5	7.9 km
sub2	286/284	37/35	5/4	1.9 km
sub3	284.5/284	36.5/35.75	5/8	0.95 km
sub4	284.288881/284.220387	36.248712/36.108466	1/10	0.15 km

Table 2 WAM run data

Description	basin	region	sub1	sub2
Propagation time-step	12 min	6 min	2 min	1 min
Source time-step	12 min	6 min	2 min	1 min

of a nested WAM computation (here the sub3 nest) would produce more accurate nearshore wave conditions than applying WAM in the same nest. The improved accuracy would be achieved by accounting for triad wave-wave interactions and depth-induced wave breaking processes included in the SWAN code but not in the WAM code. Thus, coupling the WAM and SWAN codes in the finest nest would combine the respective deepwater and shallow-water strengths of the two codes resulting in more accurate nearshore wave conditions.

The length of the nest sides, the mesh sizes, and the number of cells are as follows: for the sub2 nest, 182.0 km x 222.2 km, 5/4-minute resolution, 96x96 cells; for the sub3 nest, 45.1 km x 83.3 km, 5/8-minute mesh resolution, 48x72 cells; and for the sub4 nest, 6.1 km x 15.6 km, 1/10-minute mesh resolution, 41x84 cells. The boundary condition spectra for the sub3 nest were obtained from the WAM run on the sub2 nest. The purpose of adding subregions sub3 and sub4 was to obtain sufficient resolution for the FRF test site located near the shore (8-m array, 900 m).

3.2 Mesh generation

In the SWAN code, the user supplies the length of the sides (in meters) of the computational grid and the number of cells in each direction. For the bathymetry and wind fields, the user supplies the spatial step size and the number of cells. The longitude and latitude of the southwest corner point must also be given. When using the WAM/SWAN interface, the following relations, not given in the SWAN USER Manual, must be used to convert the WAM nest defined in degrees to a SWAN nest

defined in meters; otherwise, the WAM boundary spectra will be incorrectly placed on the SWAN mesh. The SWAN grid node spacings and lengths of the sides of the computational grid must be generated using the equations

$$\Delta x = F * \Delta longitude_d * \beta \tag{5}$$

and

$$\Delta y = F * \Delta latitude_d \tag{6}$$

where

$$\beta = cos(\frac{\pi}{180} * latitude_d) \tag{7}$$

and

$$F = \frac{Earth's\ circumference\ at\ the\ equator\ (meters)}{360} \tag{8}$$

where the subscript "d" denotes degrees. The Earth's circumference at the equator was taken as 40,000,000 meters. The factor β accounts for the variation with latitude of the length (in meters) of a fixed increment of longitude (in degrees) due to the Earth's curvature.

For WAM, the user supplies the maximum and minimum values and the step size in the longitude and latitude directions in degrees. These data are given in Table 1. On the sub2 nest, the Cartesian wave propagation option present in the WAM code was used.

3.3 Model couplings

Table 3 shows the the different coupled deployments of the WAM and SWAN codes used in this study. The WAM and SWAN runs on the different nests are coupled to WAM (or SWAN) through the boundary spectra that were created by a previous coarse-grid WAM (or SWAN) run.

During the basin computation, predicted wave spectra are interpolated to the boundaries of the region and saved. Likewise, during the computations for the region, spectra are interpolated to the boundaries of subregion sub1 and saved; a similar procedure is followed for the sub2 nest. The boundary spectra for the SWAN sub3 nest were obtained from the WAM run on the sub2 nest. The boundary condition spectra, the winds, and the bathymetry drive the computations for the different nests.

Table 3 Types of coupling

Nest level	Type of coupling	Propagation scheme
basin	none	spherical
region	WAM-WAM	spherical
sub1	WAM-WAM	spherical
sub2	WAM-WAM	spherical
sub2	WAM-WAM	Cartesian
sub2	SWAN-WAM	Cartesian
sub3	SWAN-WAM	Cartesian
sub4	SWAN-SWAN	Cartesian

4 Input and evaluation data

4.1 Bathymetry

The bathymetry data for the basin and region were supplied by Jensen [10]. The bathymetry for the sub1, sub2, and sub3 nests was downloaded from the Naval Oceanographic Office (NAVO) variable resolution gridded bathymetry database (DBDBV) [14]. The maximum precision of the DBDBV database is 5/8-minute (approximately 1 km at the equator) with depths rounded to the nearest meter before being written to the downloaded file. To obtain a more accurate bathymetry for the nearshore test sites, the bathymetry for the sub4 nest was taken from a database with 1/10-minute precision with no depth rounding. These data, from Herbers [8], were obtained using a combination of hydrographic survey data and surveys conducted at Cape Hatteras during the Duck94 experiment (see http://www.frf.usace.army.mil). It would have been preferable to have used only one database, but this was not possible since the 1/10-minute precision bathymetry only covers a small subset of the nest sub2.

4.2 Hindcast wind fields

The hindcast wind fields used to drive the WAM and SWAN computations nests were provided by Jensen[10]. The method used to generate the wind data is described by Cox et al. [5]. The wind fields are defined on the basin nest, which has a 30-minute mesh resolution and are interpolated to the region and subregion nests using bilinear surface interpolation.

4.3 Data observations

The test sites are located in the Atlantic Ocean, along the outer banks of North Carolina and the coast of Virginia. The SWAN and WAM computations are compared with data from two NOAA C-MAN stations, one NOAA buoy, and two FRF test sites located at Duck, NC. These sites were selected because data were available for the September 1995 test period. Table 4 gives the latitude and longitude coordinates for the test sites and their approximate mean water depths. The water depths for NOAA buoy 44014 and the FRF 8-m array were taken from the NOAA and FRF Web sites. The water depths for NOAA stations chlv2 and dnsl2 were provided by Knoll [11]. The water depth for the FRF buoy wr630 was supplied by Long [13]. The test locations and bathymetry are shown in Figure 2, where Chesapeake Bay is indicated as "C. Bay," Albemarle Sound as "A. Sound,"

Table 4 Test site data

Test site	latitude	longitude	360 + longitude	water depth, m
NOAA buoy 44014	36.5831 N	-74.8336 W	285.1664	47.5
NOAA station dsln7	35.1533 N	-75.2967 W	284.7033	19.0
NOAA station chlv2	36.9050 N	-75.7133 W	284.2867	11.6
FRF buoy wr630	36.1681 N	-75.6999 W	284.3001	17.1
FRF 8-m array	36.1906 N	-75.7434 W	284.2566	8.0

and Pamlico Sound as P. "Sound." Water depth contours less than 50 meters are shown. NOAA buoy 44014 and test station dsln7 are situated on the edge of the continental shelf; beyond the shelf the water depth increases rapidly to 3000-4000 m. NOAA buoy wr630 is located 4 km offshore, and the FRF 8-m array is 900 m offshore.

Table 5 summarizes the types of measurements available at the different data sites. In the table, Hmo represents availability of significant wave height data, θ_{mean} represents availability of mean wave direction data, and Tmax represents availability of peak wave period data.

5 Numerical accuracy and run parameters

5.1 Mesh refinement

The effect of mesh refinement for the WAM and SWAN codes was examined. The SWAN results showed greater sensitivity to the spatial mesh size than the WAM results. The reason for this is that although WAM and SWAN both use first-order time differencing, the implicit scheme in SWAN is

Table 5 Availability of data

Instrument ID	location	Hmo	θ_{mean}	Tmax
NOAA buoy 44014	Virginia Beach, VA	yes	yes	yes
NOAA station chlv2	Chesapeake Light, VA	yes	no	yes
NOAA station dsln7	Diamond Shls. Light, NC	yes	no	yes
FRF buoy wr630	Duck, NC	yes	no	yes
FRF 8-m array	Duck, NC	yes	yes	yes

more dissipative than the explicit scheme in WAM. This is true even if both codes are run using the limiting explicit time-step. This can be shown by applying the explicit and implicit schemes to the linear wave advection equation

$$u_t + au_x = 0 \;\; ; \; a > 0 \tag{9}$$

Using Taylor series expansions shows that the modified equation being solved is

$$u_t + au_x = \nu u_{xx} \tag{10}$$

where the explicit and implicit scheme dissipation coefficients, ν, are given, respectively, by

$$\nu_{exp} = a(1-\lambda)\Delta x_{exp}/2 \tag{11}$$

$$\nu_{imp} = a(1+\lambda)\Delta x_{exp}/2 \tag{12}$$

The Courant-Fredrichs-Levy (CFL) number, λ, is defined as

$$\lambda = \frac{a\Delta t}{\Delta x} \tag{13}$$

A Von Neumann stability analysis leads to the condition $\lambda_{exp} \leq 1$; for the implicit case, there is no restriction on the time-step. Suppose one uses the explicit limit for both schemes and the component of the wave spectrum where $\lambda = 1$ is considered. For the explicit scheme, this component of the spectrum travels undamped ($\nu_{exp} = 0$), whereas for the implicit scheme, it is damped by the coefficient $\nu_{imp} = a\Delta x$. Examining another component, where $\lambda = 1/2$, the dissipative coefficients become

$$\nu_{exp} = a\Delta x/4 \tag{14}$$

$$\nu_{imp} = 3a\Delta x/4 \tag{15}$$

giving

$$\nu_{imp} = 3\nu_{exp} \tag{16}$$

The implicit SWAN scheme is, therefore, always more dissipative than the explicit WAM scheme. Since the dissipation coefficient is proportional to Δx, the numerical dissipation can be reduced with mesh refinement. The effect of the artificial dissipation in SWAN is most notable in regions of rapid change, near the storm peaks, when the u_{xx} term becomes large.

5.2 Time-steps

For both the WAM and SWAN calculations, 25 frequencies and 24 directions were used with the frequencies logarithmically spaced from 1/30 Hz to 1.1 Hz. Results for integration time-steps of 2, 6, and 12 minutes were compared (for some SWAN runs); since the differences were negligible, the 12-minute time-step was used for the results presented here. Currents were not included in either the WAM or SWAN computations. The water depths are assumed to be the mean values; tidal effects were not considered in this study.

5.3 SWAN physics options

The SWAN computational results were obtained using the WAM cycle 4 source term formulations for whitecapping, bottom friction, and quadruplet wave-wave interaction. Four separate SWAN runs were made on the sub2 and sub3 nests; the options for each run are given in Table 6. The purpose of the four runs was to delineate the effects of each process and combinations thereof. In Table 6, "quad" represents quadruplet wave-wave interaction, "triad" represents triad wave-wave interaction, and "dib" represents depth-induced breaking. Unless otherwise noted, the SWAN runs were made with the default option setup.

6 Hindcast results

Figure 3 shows the WAM significant wave height for the region on September 10th at 0-UTC,, which corresponds to the date and time of Figure 1. The sub-regions are the white boxes in Figure 3

Table 6 SWAN run options

run	quad	triad	dib
1	x		
2	x	x	
3	x	x	x
4	x		x

(only two test sites are labeled). Shown in Figure 4 are the region wind speed contours for the same date and hour.

Figure 5 shows the WAM significant wave height contours for the sub1 nest for the same date and time. The contour lines in the lower right of Figure 5 are smooth, as the deepwater bathymetry does not play a role. As the waves approach the nearshore zone, the contours began to show depth effects. In this figure, the location of the eye of the hurricane is east of the lower right portion of the figure, where the wave heights are approximately 9 m.

Figure 6 shows the SWAN significant wave height contours for the sub2 nest on September 10, 0-UTC. Also shown are the five test locations and the sub3 nest (white rectangle). Figure 7 shows the SWAN significant wave height contours for the sub3 nest on September 10, 0-UTC. The SWAN significant wave height for the sub4 nest on September 10, 0-UTC is shown in Figure 8. Also shown are the wind directions. Figure 9 shows the sub4 mesh in the vicinity of the FRF 8-m array; the figure confirms that the sub4 mesh provides adquate resolution in the vicinity of the data site.

7 Evaluation methods

The SWAN code interpolates its computations to the test site locations using bilinear surface interpolation. The WAM code outputs the values at the point nearest the test site location. To facilitate comparisons between the two codes, a WAM post processing program was written using the same bilinear interpolation method found in the SWAN code. This program was used to interpolate the WAM results to the test site locations.

The computational results from the WAM and SWAN runs were examined using the differences between the computed values and the instrument measurements expressed as root-mean-square (rms) norms. The bias in the computations relative to the instrument measurements was also examined. The statistics are computed using the difference ΔH, defined as

$$\Delta H = H_c - H_d \tag{17}$$

where H takes on the values of significant wave height, peak wave period, and the mean wave direction, and the subscripts "c" and "d" denote "computed" and "data" values. The root-mean-square norm (rms) and the bias are defined as

$$rms(H) = \sqrt{\frac{1}{N}\sum_{i=1}^{N}(\Delta H_i)^2} \tag{18}$$

and

$$bias(H) = \frac{1}{N}\sum_{i=1}^{N}\Delta H_i \tag{19}$$

where "N" is the number of evaluation points.

8 Discussion of results

8.1 Comparison of WAM and SWAN for coastal wave predictions

The terms coastal and nearshore are relative terms with imprecise definitions. The term coastal is defined here to be the region where water depth effects are starting to be important, but are not yet the dominant processes. The term nearshore is reserved for waters where depth-induced effects are the dominant processes. The first four test sites in Table 4 are in coastal waters while the fifth test site is in the nearshore region. The nearshore test site is 900 m from the shoreline - see Figure 2.

The SWAN runs on the sub2 nest were made to demonstrate that equivalent accuracy could be achieved on this relatively large grid (2°x2°)with either the WAM or SWAN codes when triad wave-wave interaction and depth-induced wave breaking are switched off in the SWAN code and the SWAN computations are made using the WAM cycle 4 formulations for whitecapping, bottom friction, and quadruplet wave-wave interaction. The SWAN computations on the sub2 nest are close to or at the limit where a Cartesian grid can be expected to produce accurate results; this is due to the omission of the Earth's curvature in the Cartesian projection. The mesh size for the sub2 nest (5/4-minute resolution) is appropriate for coastal waters, but not appropriate for the nearshore zone, where length scales of wave variation are much smaller due to significant refraction, shoaling, and depth-induced breaking.

8.1.1 Nest sub2: Results for NOAA buoy 44014

Figures 10-12 show comparisons of the WAM and SWAN results for the computed significant wave heights, the mean wave directions, and the peak wave periods over the 10-day evaluation period for the sub2 nest. Also shown are NOAA buoy 44014 measurements as well as the rms and bias values. In these figures, WAM and SWAN show similar levels of accuracy. Because NOAA buoy 44014 is situated in a water depth of 47.5 meters, depth-induced wave breaking does not play a role, and the two codes should produce similar results. To three decimal places, there were no differences in the SWAN results for the different runs given in Table 6. It should be noted that the nautical convention for wave and wind directions is used in this paper; that is, the direction to where the vector points, measured clockwise from the positive latitude-axis.

Figure 13 shows the Hmo/depth ratios at the different test sites computed from the buoy measurements. This ratio is a good indicator of when depth-induced breaking will occur. The ratios are small ($\approx .08$) at NOAA buoy 44014, confirming deepwater wave behavior.

Figure 10 shows the time phase difference for significant wave height to be approximately the same for both codes and quite noticeable. Figures 11 and Figure 12 indicate that the peak wave period and mean wave direction are predicted equally well by both models and compare favorably with the data. Figure 14 shows Figure 10 replotted with the time of the computations shifted 12 hours ahead. One can estimate from Figure 14 that the computed significant wave heights at NOAA buoy 44014 are lagging the measurements by approximately 12 hours. The phase lag is not as evident in the peak wave period or the mean wave direction.

The wind speed and direction at NOAA buoy 44014 were examined to determine whether the lagging behavior observed at NOAA buoy 44014 could be due to the local wind fields. Shown in Figure 15 is a comparison between the wind speed used in the SWAN runs and the buoy measurements; Figure 16 shows a close-up of the comparison for the period September 9-12. There is relatively good agreement between the two time series that suggests that local wind errors are not causing the wave height lag. It would, therefore, appear that the lag is either due to phase errors in the offshore wave predictions, related to the errors in the spatial location of the hurricane, or wave group velocity errors during the propagation of waves from the vicinity of the hurricane to the coastline. These errors are then passed to the next nest through the boundary spectra.

Examining the significant wave height contours for September 10, 0-UTC, (Figure 3), one can infer offshore phase lag. The deduced eye location appears to lag the NOAA data and to be displaced east of the NOAA data. The wind field for the same day and hour does not show a lag, but does show the eye to be located to the east of the NOAA data. The significant wave heights and wind fields for September 8-9 did not exhibit the lag behavior. This is reflected in Figure 17, which shows

the location of the eye of the hurricane for the period September 8-11, obtained from the wave height and wind speed contours and the NOAA data. After September 10th, it was difficult to determine the eye from the significant wave height contour plots; therefore, these points are omitted from the plot. Figure 17 shows that the agreement between the eye location obtained from the winds and the NOAA data gradually degrades after September 9, 0-UTC. The deteriorating agreement corresponds to a period of rapid hurricane movement, which would magnify source term and propagation errors in both the wind and hindcast calculations. One method to correct this would be to use a smaller propagation step when the solution is changing rapidly or perform sub-iterations at each time-step; however, this is not a feature of the current version of WAM cycle 4.

There are two possible explanations for the differences observed between the significant wave height computations and measurements at NOAA buoy 44014. First, it is known that the first-order explicit scheme applied to the linear wave equation has a lagging phase error for Courant-Fredrichs-Levy (CFL) numbers less than 1/2 (see Tannehill et al. [17]) and a leading phase error for CFL numbers greater than 1/2. The explicit time-step for an evenly spaced grid is determined by the maximum group velocity, which would be near the eye of the hurricane in the basin and region runs. Since the group velocities for most of the field are much less than those near the eye, it is quite possible that most of the wave field is propagated with CFL numbers less than 1/2 and, therefore, lagging phase errors. A third and more likely cause was put forward by Jensen [10], who noted that the computed significant wave heights at NOAA buoy 44014 for the period September 6-9 do not agree well with the measurements. This may indicate that another storm was present in the region, somewhere between the hurricane and the U.S. coastline, which is not accounted for in the wind fields.

8.1.2 Nest sub2: Results for NOAA station chlv2

Figures 18-19 show comparisons between computed significant wave heights and peak wave period and the NOAA station chlv2 measurements. In Figure 18, WAM and SWAN show similar trends for the significant wave height with SWAN yielding better accuracy; both codes overestimate the significant wave height at the peak of the storm. Figure 19 shows that the peak wave period is predicted equally well by both codes. At the peak of the storm, the Hmo/depth ratio is $\approx .16$. The differences in the SWAN results for the different runs given in Table 6 were in the third decimal place. The agreement between the WAM and SWAN codes is very good, but the agreement with measurements deteriorates after September 9. Shown in Figure 20 is a comparison between the wind speed used in the SWAN runs and the buoy measurements. In this figure, the agreement seems reasonable. However, in Figure 21, which shows the comparison for the period September 9-12, the

trend in the hindcast winds over the first six hours of day 9 is different from the data. Likewise, there are large differences over day 10. Thus, the differences between the wave computations and the measurements starting at day 9 may be related more to errors in the input winds rather than the physics in the WAM and SWAN codes.

8.1.3 Nest sub2: Results for NOAA station dsln7

The WAM and SWAN results at NOAA buoy 44014 and NOAA station chlv2 showed very good agreement, which was expected, due to identical source terms and propagation method selection. Good agreement was also expected at NOAA station dsln7. However, Figures 22 and 23, which show comparisons between computed significant wave heights and peak wave periods and the NOAA buoy dsln7 measurements, show poor agreement. These figures show WAM to be the more accurate for the wave heights with SWAN underpredicting the wave heights. The phase behavior for significant wave height is approximately the same for both codes, with a phase difference at the maximum wave height of approximately 12 hours. This case illustrates that even when WAM and SWAN use the same source term formulations for whitecapping, bottom friction, and quadruplet wave-wave interaction, the codes produce different results due to implementation strategies, minor differences in coefficients, and differences in the numerical algorithms used in geographical space.

Shown in Figure 24 is a comparison between the wind speeds used in the SWAN runs and the buoy measurements. Figure 25 shows the comparison for the period September 9-12. Figure 24 and Figure 25 show, in general, large errors in the hindcast winds over the 10-day evaluation period; the resulting poor agreement between the wave-wave computations and the measurements is not surprising.

8.1.4 Nest sub2: Results for the FRF buoy wr630

Figures 26-27 show comparisons between the computed significant wave heights and peak wave periods and buoy measurements at the FRF buoy wr630. In Figure 26, the two models' significant wave heights are approximately the same until the peak of the storm. Shown in this figure are the SWAN values of rms and bias for both the sub2 and sub3 nests. It is not clear whether the differences between the sub2 and sub3 nests are related to the increased spatial resolution or the more accurate water depths in the sub3 nest. Figure 27 shows that the peak wave period is predicted equally well by both codes. The differences in the SWAN results for the different runs given in Table 6 were again in the third decimal place. Neither WAM nor SWAN were able to predict the variation of peak period after September 10. In general, the agreement between the WAM significant wave height on the sub2 nest and the SWAN significant wave height on the sub3 nest is good. Winds measurements

at NOAA buoy wr630 were not available for analysis.

8.2 Coupling of WAM and SWAN for nearshore wave predictions

8.2.1 The effect of mesh refinement on the SWAN results

Figure 28 shows comparisons for the significant wave height for the WAM and SWAN codes as the mesh is refined for the SWAN computations. Only quadruplet wave-wave interaction is accounted for, and both codes use the same formulations for the source terms. Under these conditions, both codes should produce the same results. For clarity, the measurements are not shown. This figure shows the sensitivity of the SWAN results to the mesh used. As the mesh is refined, the SWAN results approach the WAM results on the sub2 nest. The mesh sensitivity for the SWAN computations reflects the larger dissipative character of the SWAN numerical algorithm, as noted in Section 5.1. The rms and bias values shown in this figure are those for the period September 3rd to September 9th. This period is before the storm's peak; the storm's peak has been omitted since the SWAN results would be closer to the data at that time, due to larger dissipation, resulting in misleading smaller rms values. From Figure 28, it is clear that the WAM/SWAN coupling cannot be done at the sub2 nest level because of the large differences in the significant wave height on that grid. The differences between the WAM results on the sub2 nest and the SWAN results on the sub3 nest are very small. The sub3 nest was chosen as the grid on which to examine the effect of improved nearshore physics on the SWAN results presented in Section 8.2.2. The differences between the sub3 nest and the sub4 nest (not shown) were small. If deemed necessary, the sub3 nest mesh size (5/8-min) could be replaced with the sub4 nest mesh size (1/10-min).

8.2.2 Effect of improved nearshore physics

This section examines the question of whether nearshore accuracy can be improved by coupling the WAM and SWAN codes; that is, whether the use of the SWAN code on the finest nest of a nested WAM computation would result in more accurate nearshore wave conditions than the use of WAM on the same nest. The SWAN code accounts for triad wave-wave interactions and depth-induced wave breaking, both of which are neglected by the WAM code. If the combined effects of these processes are significant in the nearshore zone, the use of SWAN is likely to improve predictions.

Table 7 gives the rms and bias values for the different SWAN physics options, with mesh refinement, over the period September 3rd to 10th.

Figure 29 shows a comparison between the SWAN results using only quadruplet wave-wave interaction physics and those using quadruplet wave-wave interaction and triad wave-wave interaction

Table 7 FRF 8-m array: Mesh refinement effects on the SWAN results

	Hmo (rms)		
nest	quad	quad+triad	quad+bre
sub2 (WAM)	0.118	-	-
sub4 (SWAN)	0.129	0.129	0.130
sub3 (SWAN)	0.136	0.136	0.138
sub2 (SWAN)	0.229	0.253	0.230
	Hmo (bias)		
sub2 (WAM)	-0.031	-	-
sub4 (SWAN)	-0.034	-0.034	-0.035
sub3 (SWAN)	-0.064	-0.048	-0.065
sub2 (SWAN)	-0.199	-0.046	-0.200

combined. As can be seen in this figure, the differences are negligible.

Figure 30 shows the effect of depth-induced wave breaking on the SWAN results at the FRF 8-m array. The onset of depth-induced breaking can be seen on September 9. The inclusion of depth-induced breaking reduced the maximum significant wave height by 20 percent at the FRF 8-m array.

Shown in Figure 31 is a comparison of the computations and the measurements for the mean wave direction. On average, the computations underestimate the measurements by 28 degrees. Figure 32 shows the same comparison for the peak wave period.

In order to further understand the poor agreement between the computations and the measurements beginning September 9th, the winds at the FRF 8-m array were examined. Shown in Figure 33 is a comparison between the wind speeds used in the SWAN runs and the buoy measurements. Figure 34 shows the comparison for the period September 9-12. These figures show, in general, large errors in the hindcast winds over the 10-day evaluation period and in particular, over the period September 9-12. Thus, it appears that the poor agreement over this period reflects errors in the hindcast winds. This is in agreement with the findings of Section 8.1.3, and clearly further studies are needed with more accurate wind fields.

9 Conclusions

The WAM/SWAN wave model boundary condition interface option present in the SWAN Version 40.01 code has been tested, and WAM and SWAN predictions have been compared with measurements at five test sites. The SWAN self-nesting option has also been tested. The selected test case was a simulation of wave activity during 1995 Hurricane Luis for which NOAA buoy data were available as well as data from the FRF at Duck, NC. A six-nest simulation was performed. WAM was run on the four coarsest nests; SWAN was run on the three finest nests. The purpose of this study was to determine the effectiveness of applying SWAN, a model developed specifically for coastal and inland waters, on the finest WAM nest as a means of obtaining more accurate nearshore wave predictions. The following conclusions were reached:

1) With the exception of NOAA station dsln7, the results for the WAM and SWAN codes showed good agreement when the triad wave-wave interaction and depth-induced wave breaking processes in the SWAN code were switched off and both codes used the WAM cycle 4 formulations for whitecapping, bottom friction, and quadruplet wave-wave interaction. For these options, both codes should theoretically produce the same results.

2) The computed peak of the storm lagged the measurements by approximately 12 hours. This was most evident at NOAA buoy 44014. Two possible causes were put forth: 1) A lagging phase error present in the WAM numerical solutions on the basin and region nests that was passed to the finest nests through the boundary spectra. This lagging phase error may be caused by the first-order accurate time scheme, or may have occured during the period of rapid hurricane movement, which would magnify source term and propagation errors in both the wind and wave calculations. If the latter is the cause, one remedy would be to use a smaller propagation step when the solution is changing rapidly, or to perform sub-iterations at each time-step; 2) The lag may be the result of another storm present in the coastal region in the three days preceeding the storm's peak, somewhere between the hurricane and the U.S. coastline, that is not accounted for in the wind fields.

3) In general, the agreement between the wave computations and measurements for NOAA stations chlv2 and dsln7, NOAA buoy wr630, and the FRF 8-m array was poor after September 9. Comparison of the input winds and measurements at NOAA stations chlv2 and dsln7, and the FRF 8-m array showed significant errors in the hindcast winds, which may be the cause of the poor agreement. The most serious error was the failure to correlate periods of increasing and decreasing winds.

4) In general, the WAM results were more accurate than the SWAN results for the same mesh. This was very evident for the nearshore FRF 8-m test results where a finer mesh was required by SWAN

to achieve the same accuracy as the WAM code.

5) The WAM code is not well suited for fine mesh computations for the following reasons: As the mesh is refined, the propagation time-step required in WAM can become smaller than one minute, which is the limiting value for the WAM date stamp. A second limitation of the WAM code is that bathymetry values must be integers (1,2,3,... etc.). This can lead to a significant loss of bathymetry definition for regions with small variations in bathymetry. Third, for small propagation time-steps, the size of the boundary condition spectra files becomes extremely large, since the boundary spectra must be interpolated and written to a file for every time-step.

6) The effect of the inclusion of depth-induced wave breaking in the SWAN code was to reduce the maximum significant wave height by 20 percent at the storm's peak at the FRF 8-m test site. This resulted in the most accurate prediction of the peak wave height among all the SWAN and WAM runs.

7) SWAN and WAM predict the peak wave period and the mean wave direction equally well.

8) A parallel version of the SWAN code is needed. The lack of computational efficiency in the SWAN code is offset somewhat by the fact that it need only be used in the finest nest of a nested WAM run.

9) The need for test data to validate nearshore depth-induced wave breaking is evident. To obtain these data, a test site would need to be situated in approximately 4 m of water so that wave breaking data from smaller more common storms could be obtained. Ideally, one would want data at an 8-m depth test site, before the onset of significant depth-induced breaking, and data at a 4-m depth test site, after wave breaking has occurred.

10) Further studies are needed, but applying the SWAN code on the finest WAM nest appears to be an effective means to obtain more accurate nearshore wave predictions.

10 Acknowledgments

This work was supported in part by a grant of computer time from the Department of Defense High Performance Computing Modernization Program at the U.S. Army Engineer Research and Development Center (ERDC) Major Shared Resource Center in Vicksburg, Mississippi. The authors would like to thank Dr. Robert Jensen of the Coastal and Hydraulics Laboratory at ERDC for suggesting and supporting this study, providing the Hurricane Luis wind fields, and making possible

the visit to ERDC of Professor IJsbrand Haagsma of the SWAN development team. The help of and many fruitful discussions with Professor IJsbrand Haagsma during his visit are greatfully acknowledged. The first author would like to thank the other members of the SWAN support team at the Delft University of Technology in the Netherlands for their help. The many discussions with Erick Rogers of Planning Systems, Inc., concerning the SWAN code were also greatly appreciated. The wind fields used in this study were developed by Oceanweather, Inc., under funding by the Atmospheric Environment Service, Canada.

References

[1] Arcilla, A. S., Roelvink, B. A., O'Connor, A. J., Reniers, H. M., and Jimenez, J. A., 1994, "The Delta flume 1993 experiment," *Proc. of Coastal Dynamic Conf.*, 488-502.

[2] Battjes, J. A., and Janssen, P. A. E. M., 1978, "Energy loss and set-up due to breaking of random waves," Proc. 16th Int. Conf. Coastal Engineering, ASCE, 569-587.

[3] Beji, S., and Battjes, J. A., 1993, "Experimental investigation of wave propagation over a bar," *Coastal Engineering*, vol. 19, 151-162

[4] Booij, N., Ris, R. C., and Holthuijsen, L. H., 1999, "A third-generation wave model for coastal regions, Part I, Model description and validation," *J. Geoph. Research* 104, C4, 7649-7666.

[5] Cox, A. T., Greenwood, J. A., Cardone, V. J., and Swail, V. R., 1995, "An Interactive Objective Kinematic Analysis System," 4th International Workshop on Wave Hindcasting and Forecasting, Banff, Alberta.

[6] Gunther, H. P., Hasselmann, K., Hasselmann S., and Janssen, P. A. E. M., 1992, "The WAM model Cycle 4," DKRZ Report No. 4, Hamburg.

[7] Hasselmann, S., Hasselmann, K., Buer, E., Janssen, P. A. E. M., Komen, G. J., Bertotti, L., Lionello, P., Guillaume, A., Cardone, V. C., Greenwood, J. A., Reistad, M., Zambresky, L., and Ewing, J. A., 1988, "The WAM model - a third generation ocean wave prediction model," *J. Physical Oceanography*, 18, 1775-1810.

[8] Herbers, T. H. C., Hendrickson, E. J., and O'Reilly, W. C., 2000, "Propagation of Swell Across a Wide Continental Shelf," *J. Geoph. Research*, accepted for publication

[9] Holthuijsen, L. H., Booij, N., Ris, R. C., Haagsma, IJ. G., Kieftenburg, A.T.M.M., and Padilla-Hernandes, R., 1999, "SWAN version 40.01 USER MANUAL,"

[10] Jensen, Robert, DoD Lead scientist, Global and Regional Wind-Wave Modeling
Coastal and Hydraulics Laboratory
U.S. Army Engineer Research and Development Center
Vicksburg, Mississippi

[11] Knoll, D., NOAA staff
National Oceanographic Data Center
Silver Springs, MD

[12] Komen, G. J., Cavaleri, L., Donelan, M., Hasselmann, K., Hasselmann, S., and Janssen, P. A. E. M., 1994, Dynamics and Modelling of Ocean Waves, *Cambridge University Press*, Cambridge.

[13] Long, C. E., Research Oceanographer
U.S. Army Field Research Facility
Duck, N.C.

[14] Naval Oceanographic Office (NAVO)
variable resolution gridded bathymetry database (DBDBV)
http://128.160.23.42/dbdbv/dbdbv.html.

[15] Nelson, R. C., 1984, "Depth limited wave heights in very flat regions," *Coastal Engineering*, 23, 43-59, 1994.

[16] Padilla, R., Osuna, P., Monbaliu, J., and Holthuijsen, L., 1998, "Intercomparing third-generation wave model nesting," 5th International Workshop on Wave Hindcasting and Forecasting, Melbourne, Florida

[17] Tannehill, J. C., Anderson, D. A., and Pletcher, R. H., 1997,
Computational Fluid Mechanics and Heat Transfer, Second Edition, Taylor and Francis.

[18] Ris, R. C., Booij, N., and Holthuijsen, L. H., 1999, "A third-generation wave model for coastal regions, Part II, Verification," *J. Geoph. Research*, 104, C4, 7667-7681.

Figure 1 Basin wind speed contours : September 10, 0-UTC

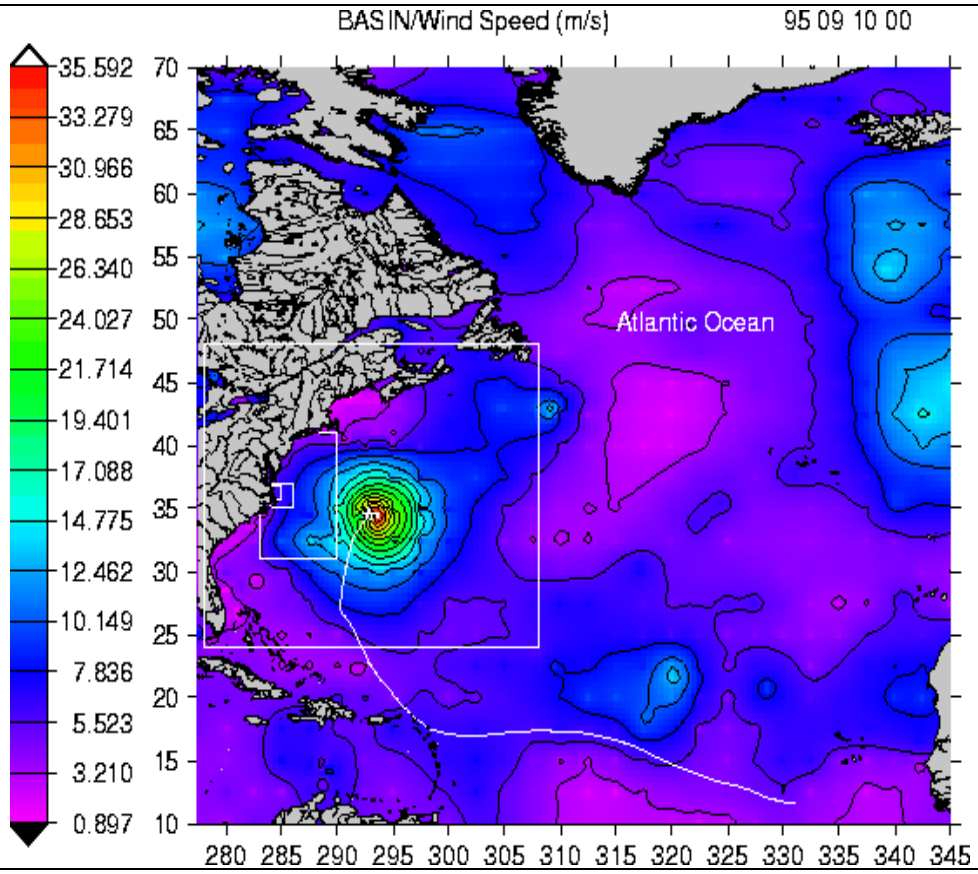

Figure 2 Bathymetry and location of buoys

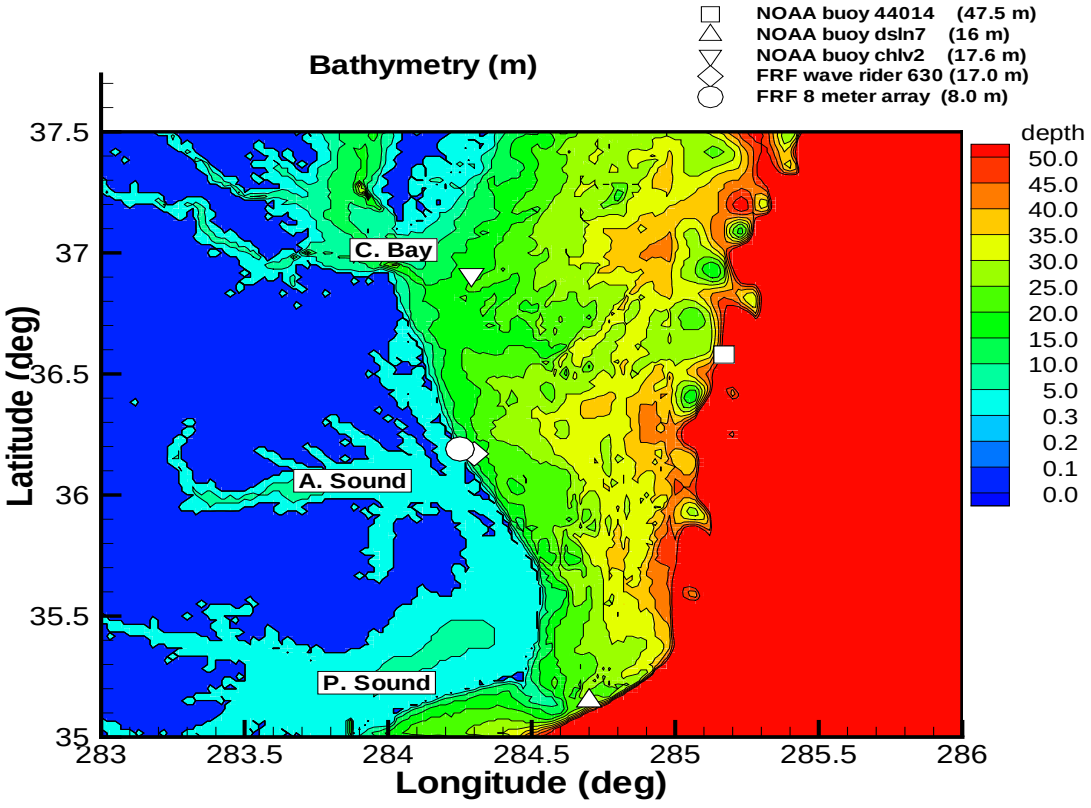

Figure 3 Region: WAM significant wave height: September 10, 0-UTC

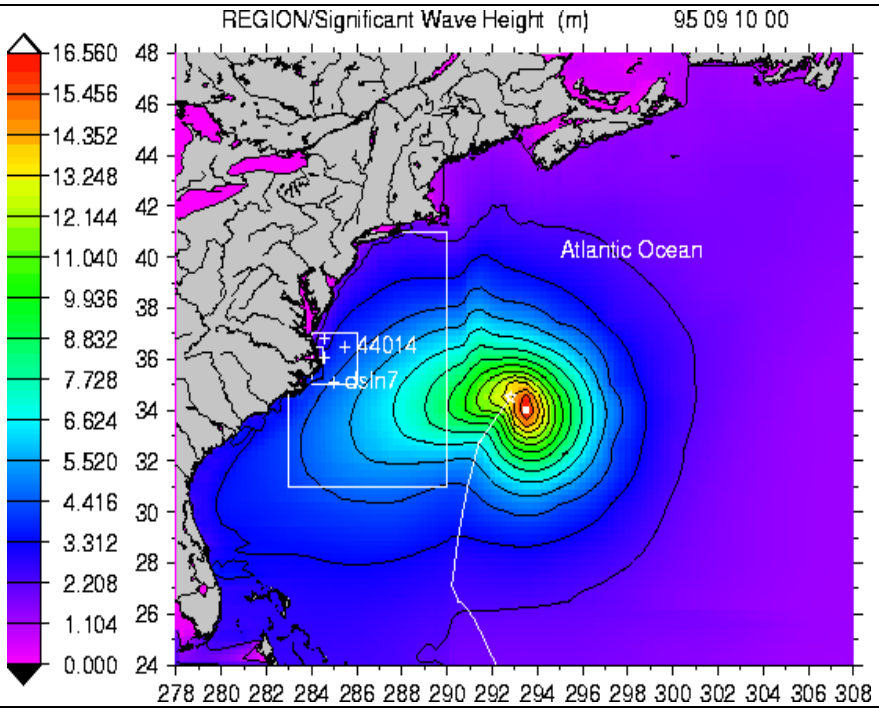

Figure 4 Region wind field on September 10, 0-UTC

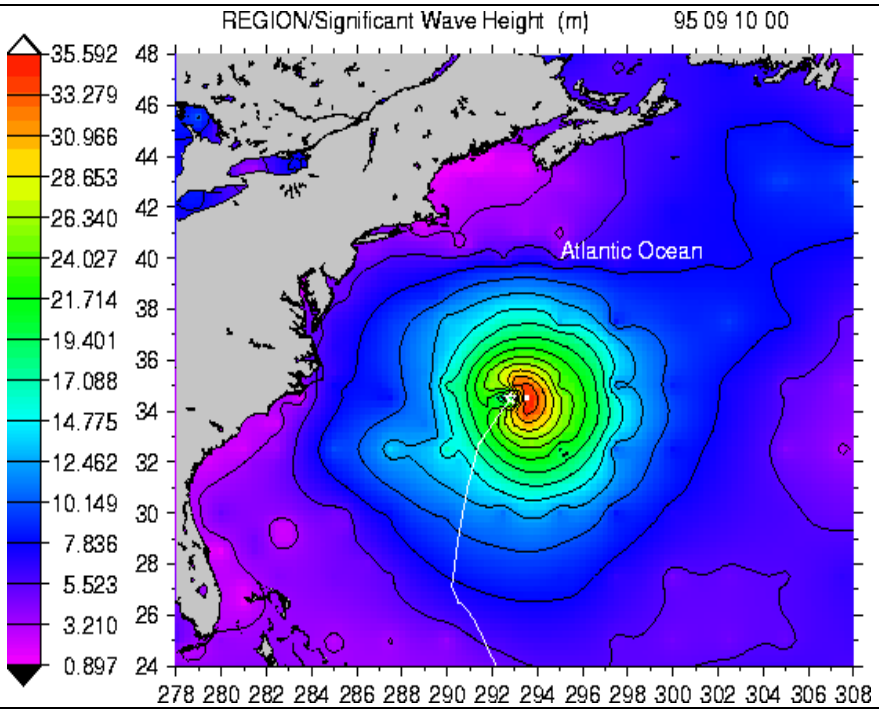

Figure 5 sub1: WAM significant wave height: September 10, 0-UTC

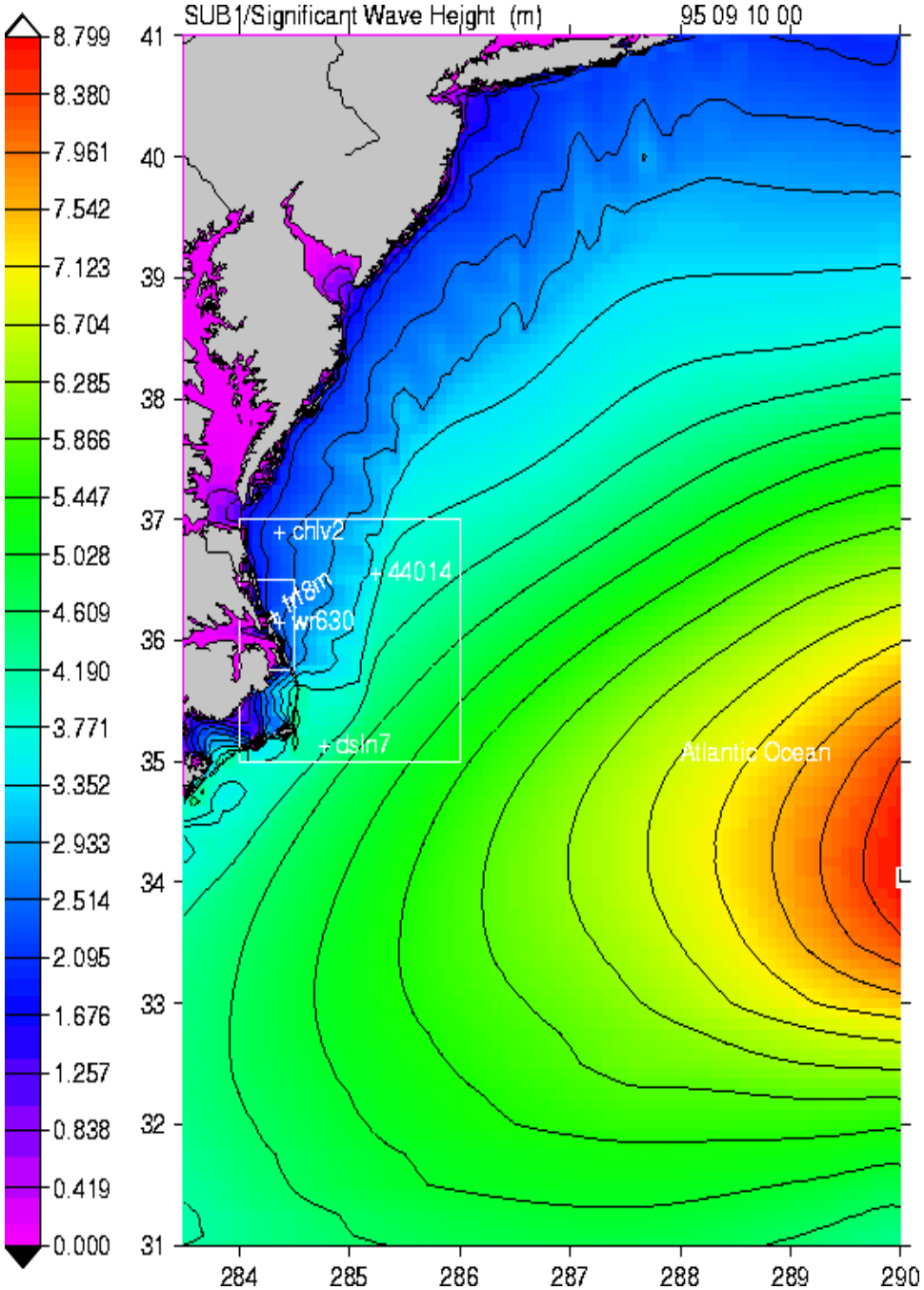

Figure 6 sub2: SWAN significant wave height: September 10, 0-UTC

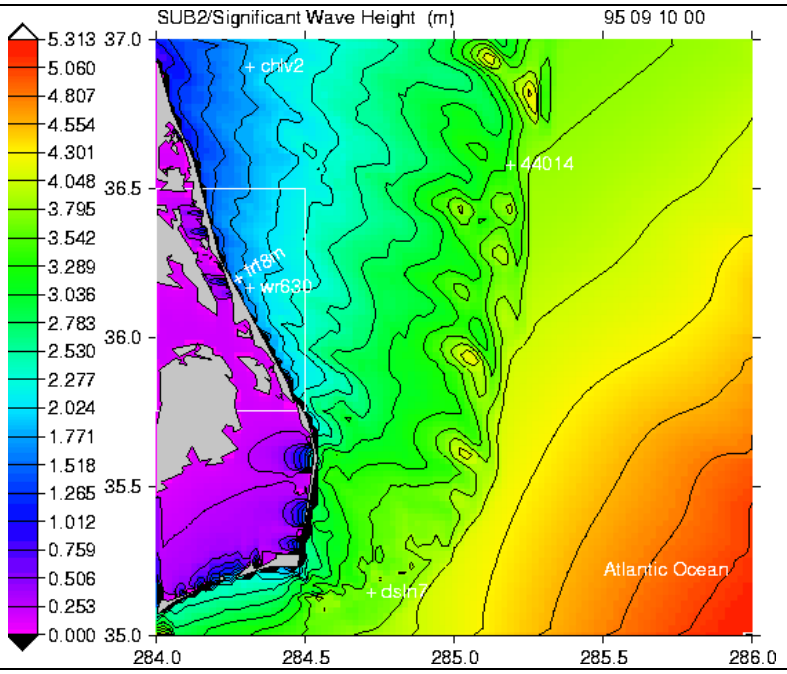

Figure 7 sub3: SWAN significant wave height: September 10, 0-UTC

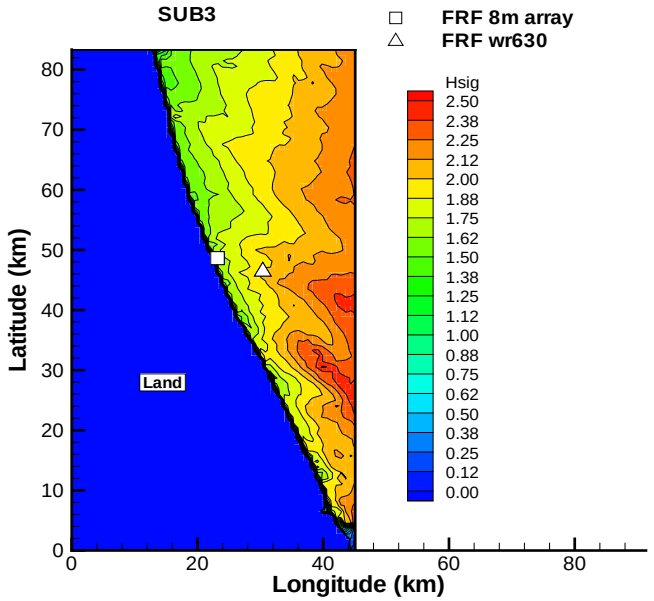

Figure 8 sub4: SWAN significant wave height: September 10, 0-UTC

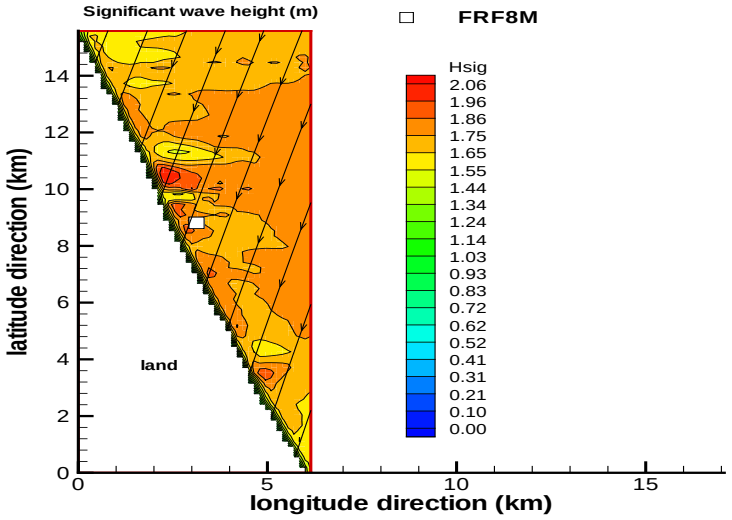

Figure 9 sub4 mesh in the vicinity of the FRF 8-m array

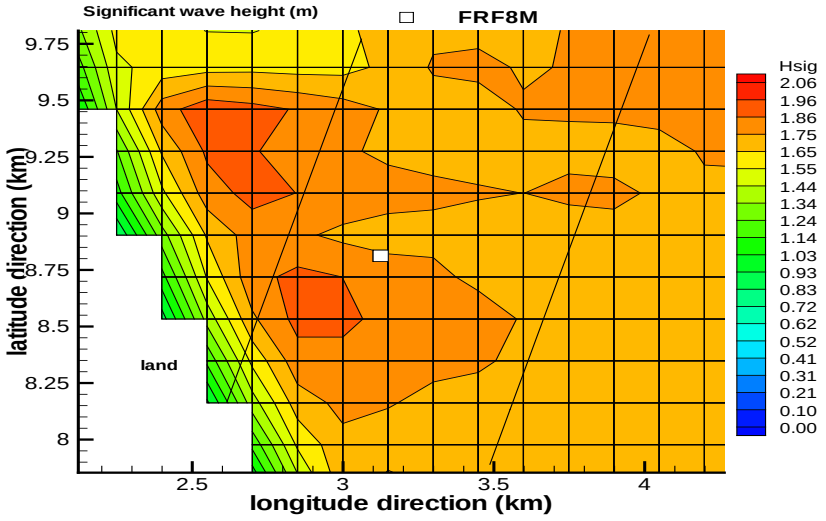

Figure 10 Time series of significant wave height: NOAA buoy 44014

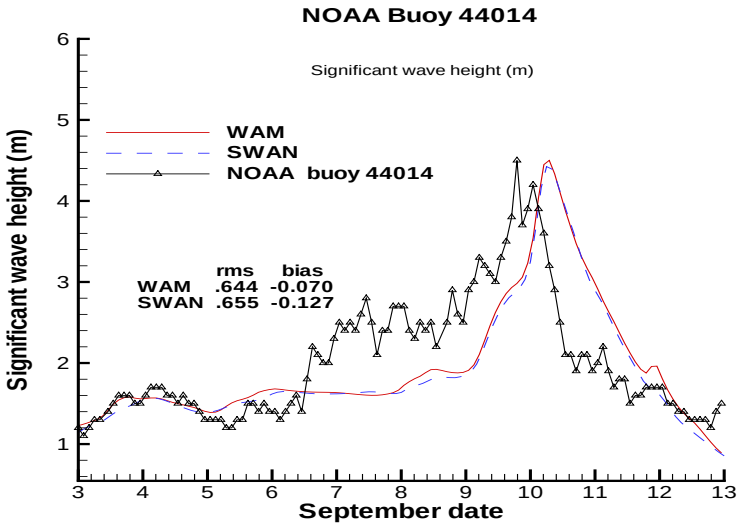

Figure 11 Time series of mean wave direction: NOAA buoy 44014

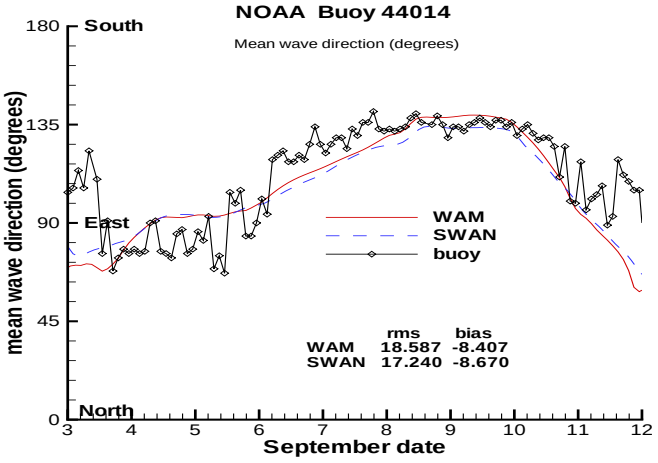

Figure 12 Time series of peak wave period: NOAA buoy 44014

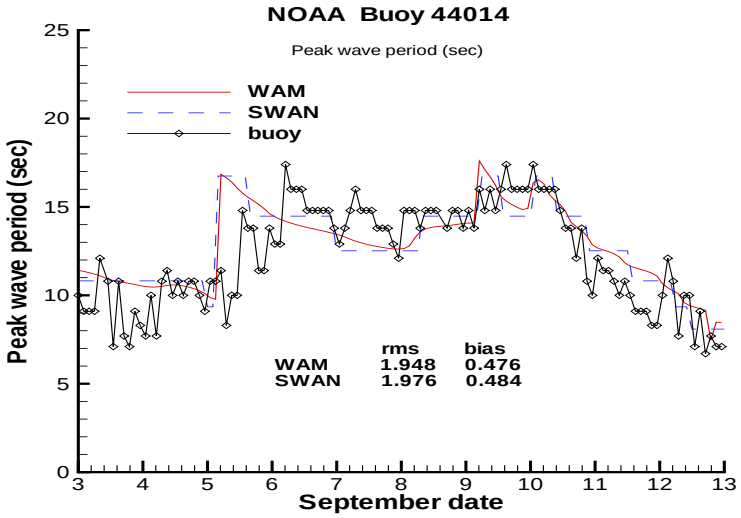

Figure 13 The Hmo/depth ratios at test sites

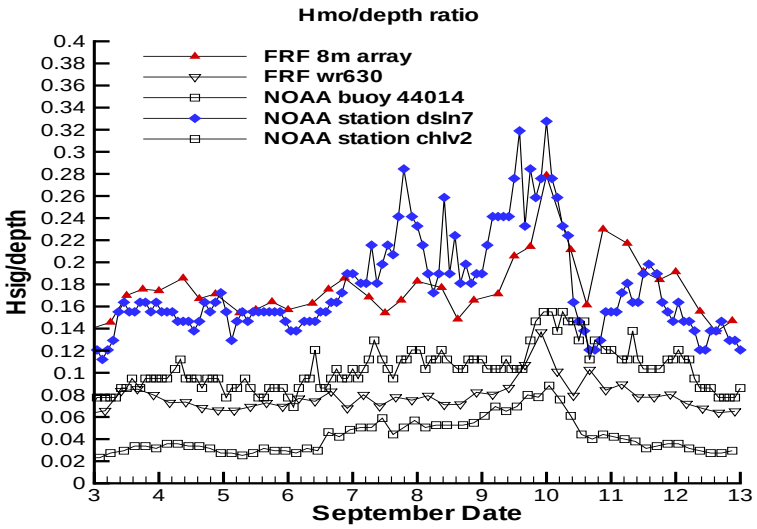

Figure 14 Significant wave height shifted 12 hrs earlier: NOAA buoy 44014

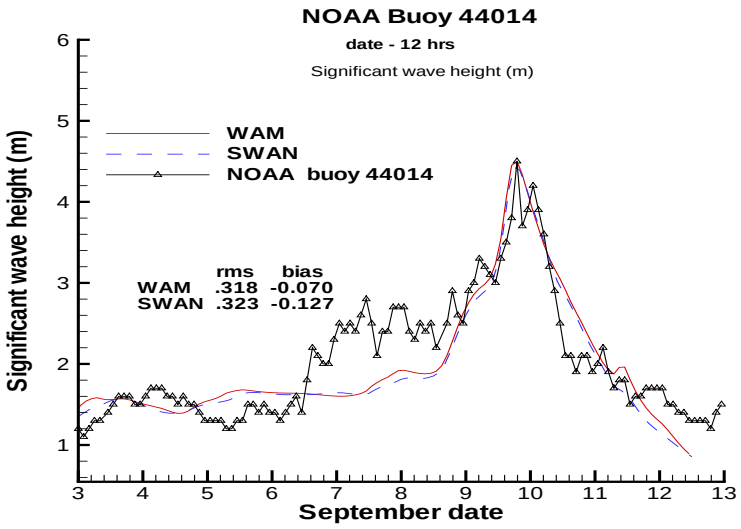

Figure 15 Comparison of input and measured wind speeds: NOAA buoy 44014

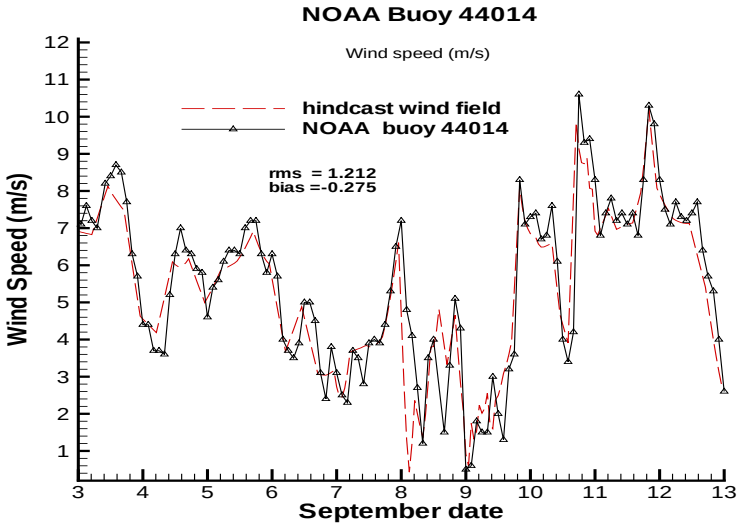

Figure 16 Wind speeds for September 9-12 at NOAA buoy 44014

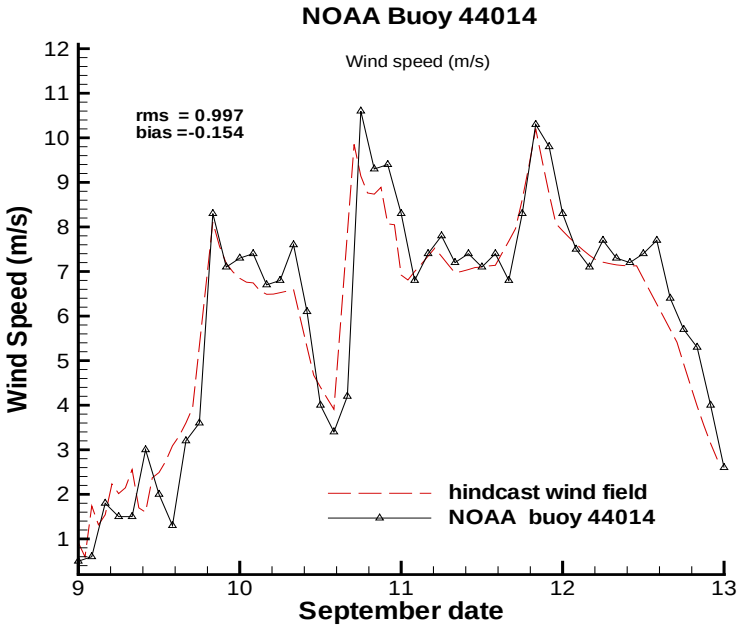

Figure 17 Track of the hurricane eye for September 7-11

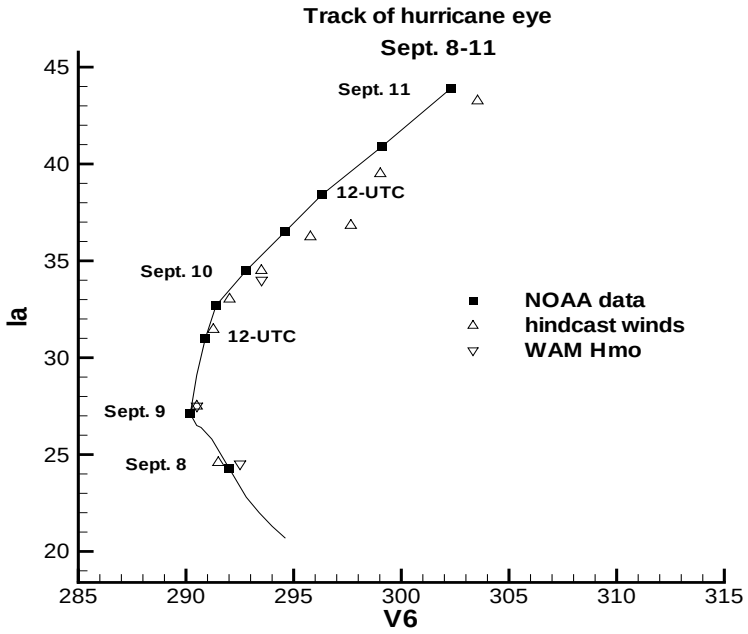

Figure 18 Time series of significant wave height: NOAA station chlv2

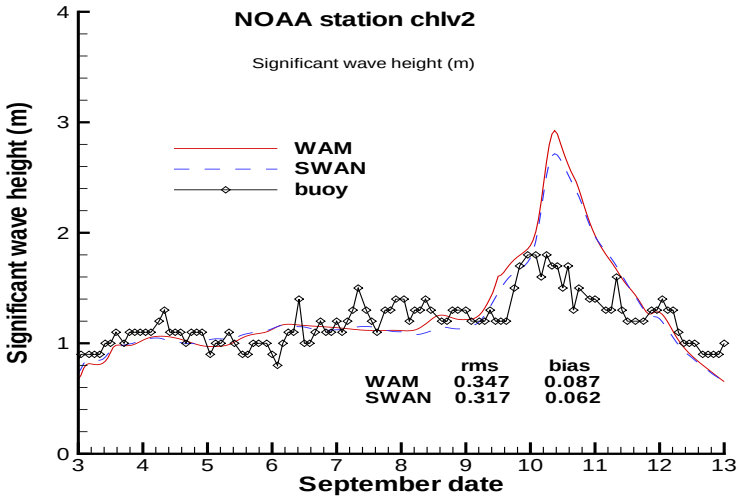

Figure 19 Time series of mean wave direction: NOAA station chlv2

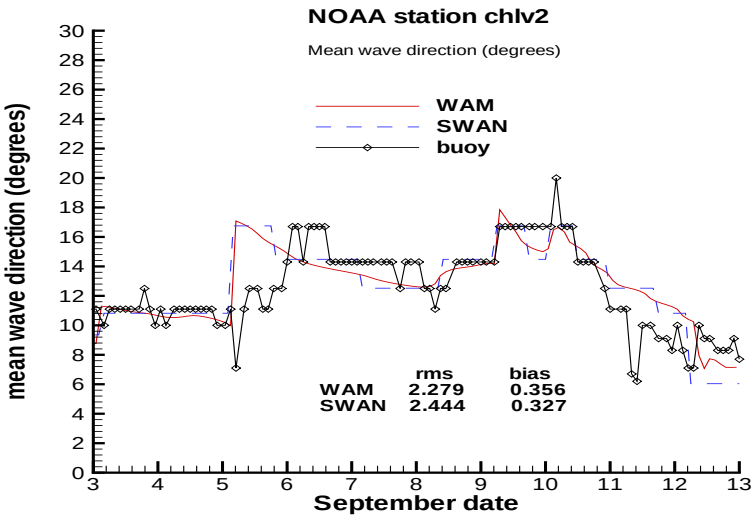

Figure 20 Comparison of input and measured wind speeds: NOAA station chlv2

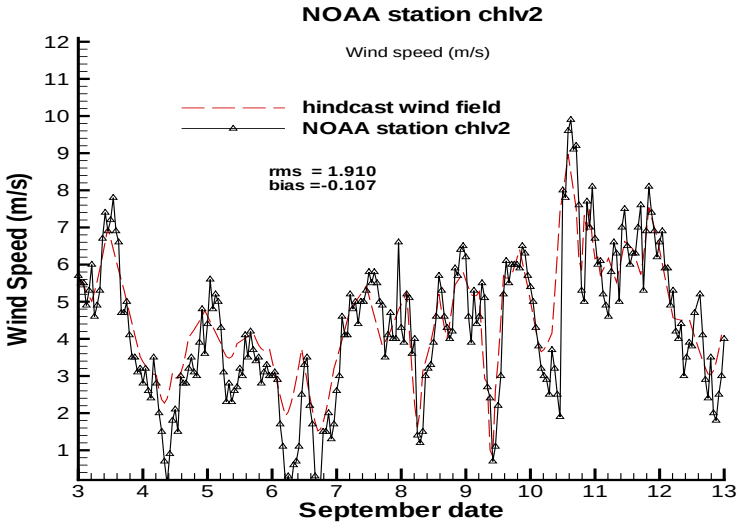

Figure 21 Wind speeds for September 9-12 at NOAA station chlv2

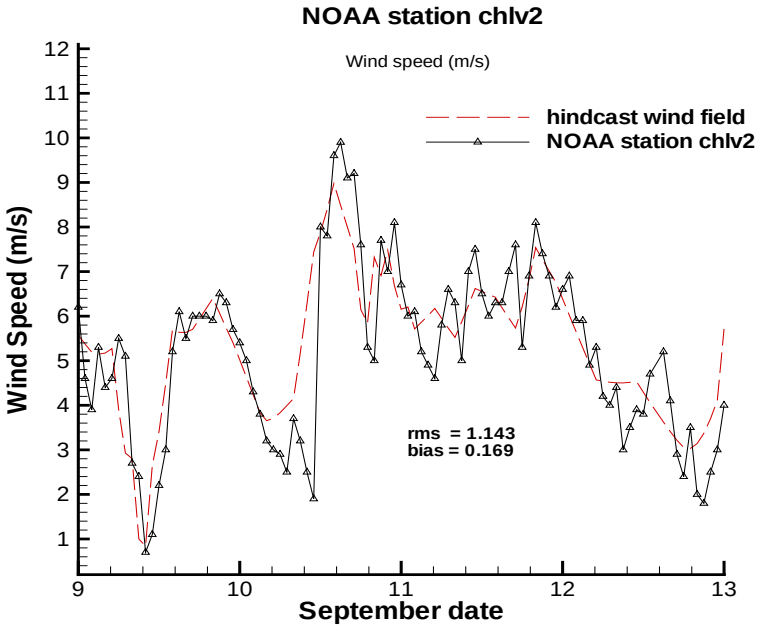

Figure 22 Time series of significant wave height: NOAA station dsln7

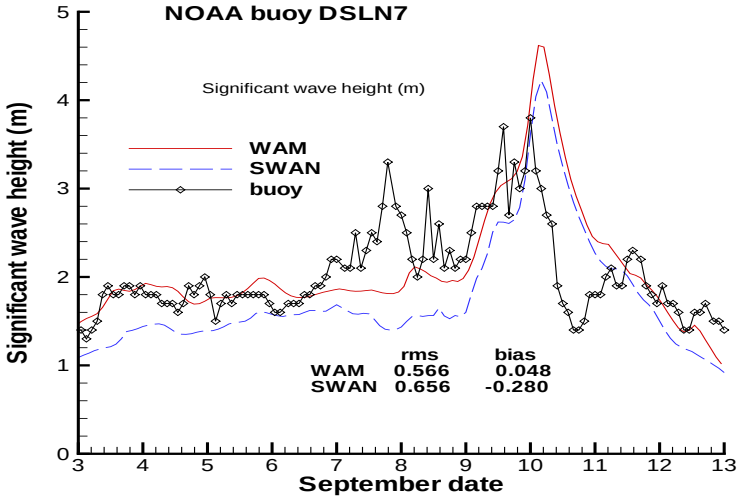

Figure 23 Time series of peak wave period: NOAA station dsln7

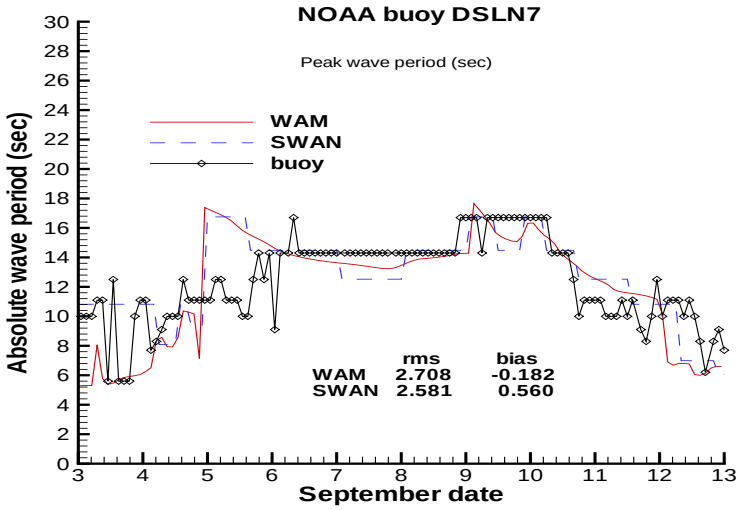

Figure 24 Comparison of input and measured wind speeds: NOAA station dsln7

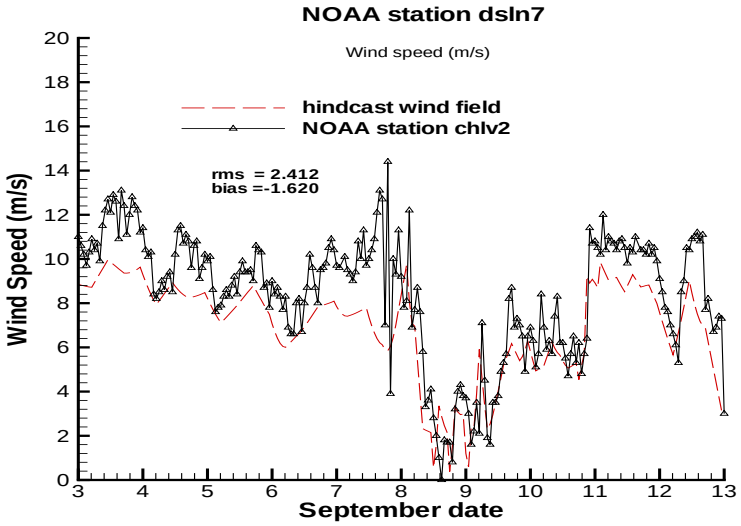

Figure 25 Wind speeds for September 9-12 at NOAA station dsln7

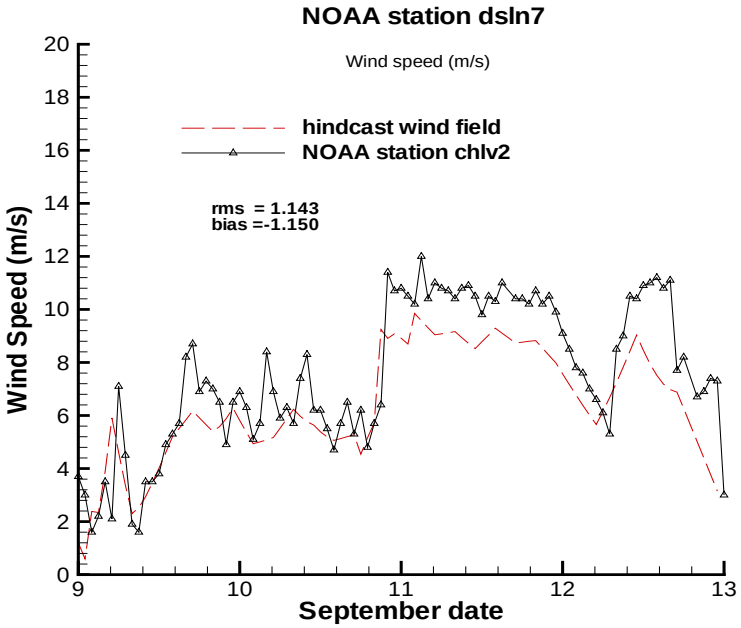

Figure 26 Time series of significant wave height: NOAA buoy wr630

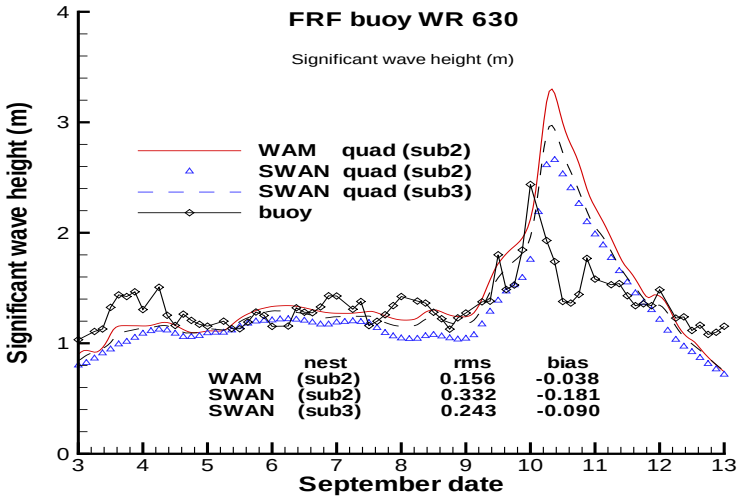

Figure 27 Time series of peak wave period: NOAA buoy wr630

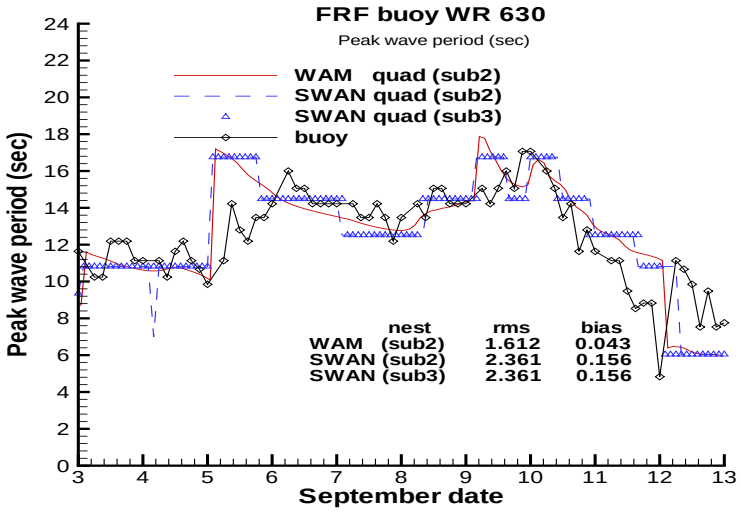

Figure 28 Effect of mesh refinement on the SWAN results for the base options: FRF 8-m array

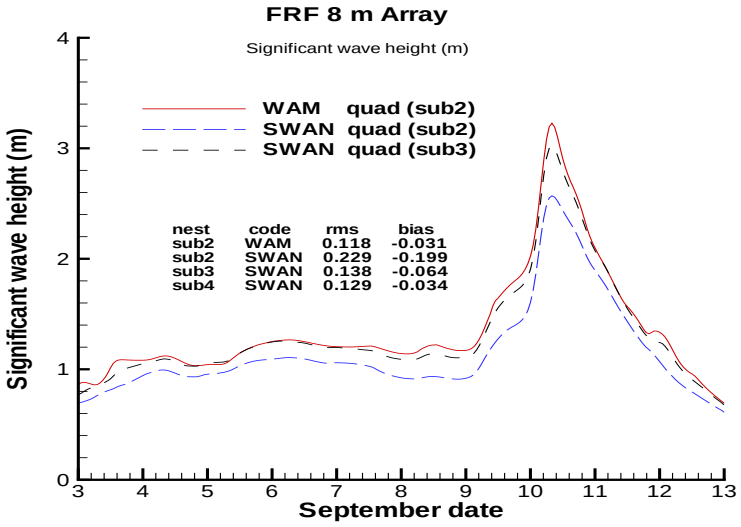

Figure 29 Effect of triad wave-wave interaction on the SWAN results: FRF 8-m array

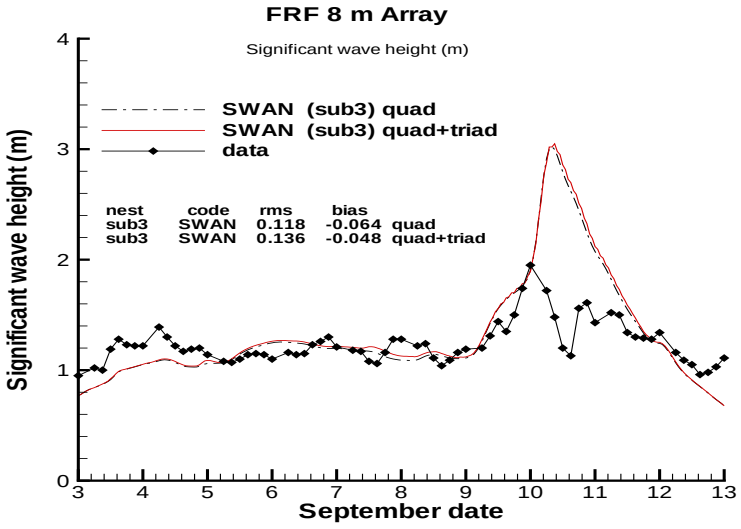

Figure 30 Effect of depth-induced wave breaking on the SWAN results: FRF 8-m array

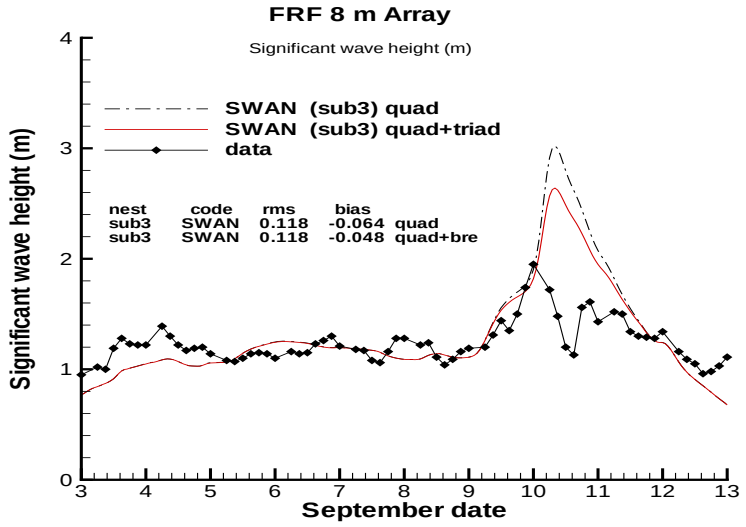

Figure 31 Time series of mean wave direction: FRF 8-m array

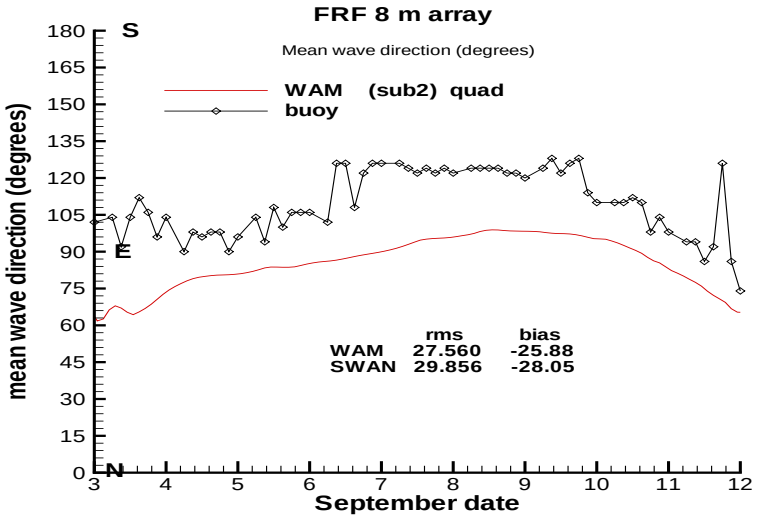

Figure 32 Time series of peak wave period: FRF 8-m array

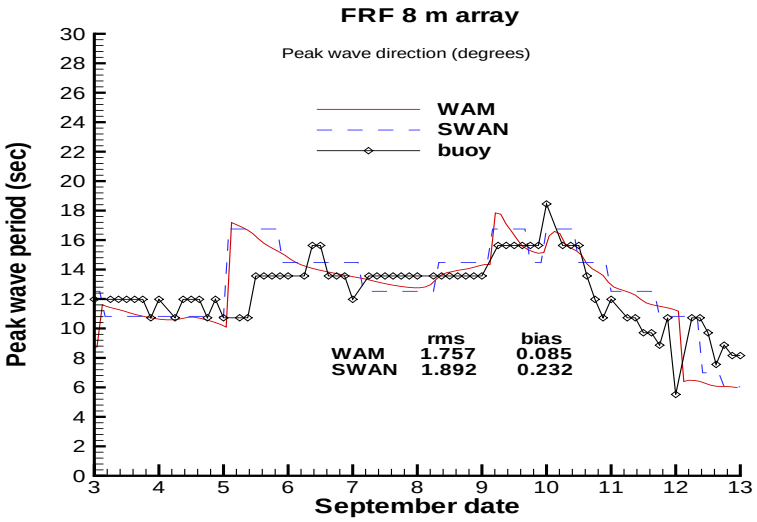

Figure 33 Time series of wind speed: FRF 8-m array

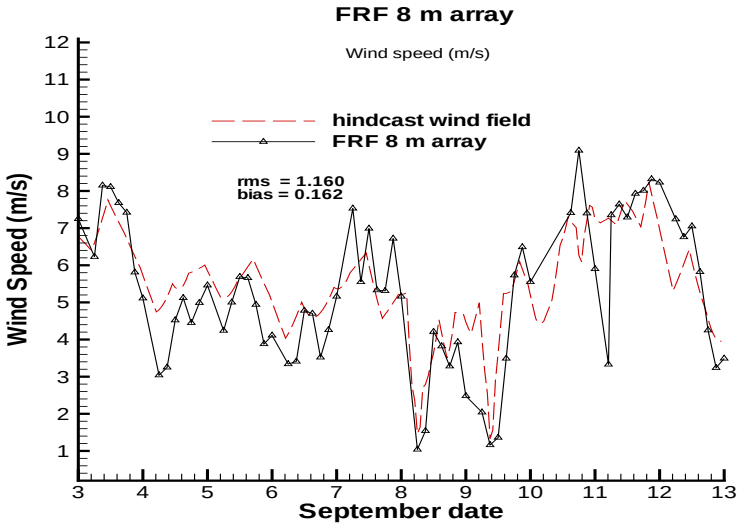

Figure 34 Wind speeds for September 9-12: FRF 8-m array